Physical Sputtering of Superconducting NbN Thin Films

Matthew Maksymowych, Luke Qi, and Erik Szakiel

June 11, 2022

Abstract

Niobium nitride (NbN) thin films are an attractive platform for various classical and quantum technologies due to their relatively high superconducting transition temperature ($T_c \sim 17$ K) and kinetic inductance fraction. Thin films of NbN are often produced via reactive DC magnetron sputtering, which allows for controlled growth of the superconducting δ-NbN phase. The properties of sputtered NbN, however, are highly sensitive to film impurities and sputtering parameters such as target power density, Ar flow rate, N_2 flow rate, substrate temperature, and substrate bias. In this work, we explore this parameter space to sputter thin films of NbN. To determine the quality of our sputtered films, we perform room temperature resistivity measurements, X-ray crystallography, and X-ray photoelectron spectroscopy. Thereafter, we pattern the films into microwave resonators which can be measured at 4 - 15 K to determine the critical temperature. This report describes our recipe for sputtering NbN and demonstrates a wide parameter window that allows for a low room temperature resistivity $\rho \sim 200$ $\mu\Omega$ -cm, a moderate superconducting transition temperature $T_c \sim 8$ K, and an internal quality factor of up to $Q_i \sim 800$. These results demonstrate a path towards high-quality superconducting films using shared tools at the Stanford Nanofabrication Facility (SNF).

Contents

1 Introduction & Background

Superconducting NbN films have been widely used in a variety of emerging quantum- and nano-devices such as superconducting nanowire single photon detectors (SNSPDs) [1, 2] and Josephson junctions [3]. Materials in the superconducting phase have zero DC electrical resistance and internal magnetic field (the Meissner effect). Unlike traditional conductors, where the current can be described by moving electrons, the electrical fluid in a superconductor consists of bound pairs of electrons called Cooper pairs [4]. Cooper pairs are crucial to the operation of SNSPDs and Josephson junctions, therefore these devices require very low temperatures well below the material's superconducting critical temperature T_c. NbN is a commonly used material for superconducting nanodevices due to its relatively high T_c. A typical value of the critical temperature of NbN is around 10 K, although temperatures as high as 17 K have been reported [5–8]. Moreover, NbN can be deposited through physical sputtering, which has much higher deposition rates compared to some other methods such as atomic layer deposition (ALD).

1.1 Reactive DC Magnetron Sputtering

Sputtering of NbN works by flowing argon (Ar) gas into an ultra-high vacuum chamber to form an Ar^+ plasma, as illustrated in Figure 1. The plasma is confined near the surface of the target material (Nb in this case) and densified by a magnetic field. A DC voltage is applied to the target which accelerates the Ar^+ ions down towards the target surface. When an Ar^+ ion bombards the target, it releases one or more atoms of Nb with relatively high kinetic energy which travel up towards the substrate. These Nb atoms collide with N_2 gas which is flowed into the chamber in order to form NbN which is then deposited onto the substrate. This process is known as reactive DC magnetron sputtering.

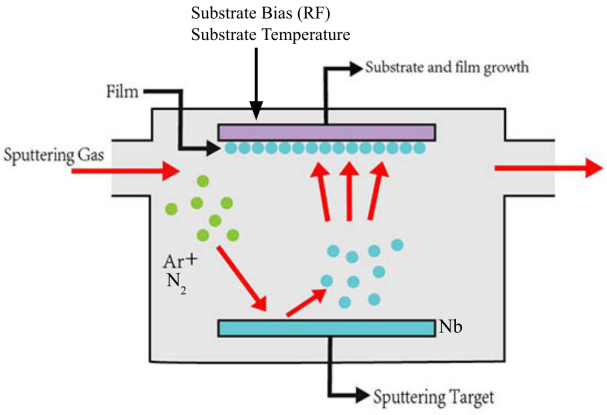

Figure 1: Diagram of the physical sputtering process for NbN deposition. Ar^+ and N_2 gas are flown in. Nb particles are ejected and deposited onto the substrate, forming a film of NbN. The RF substrate bias and temperature are two parameters that can affect the outcome of the sputtering deposition.

1.2 Sputtering Parameters

There are many sputtering parameters which affect the quality of the deposited film, including target power density, Ar flow rate, N_2 flow rate, substrate temperature, and substrate bias [7, 9]. In general, the sputtering of nitride films is most successful when using the highest target power density and lowest partial pressure of Ar possible while still maintaining a plasma in the chamber [10]. With higher power densities the target is more heavily bombarded with gas ions, resulting in higher deposition rates and more energetic Nb atoms incident upon the substrate. This also gives less time for impurities to accumulate on the deposition surface per unit thickness of NbN. With lower partial pressure of Ar, the Nb atoms incident upon the substrate have a longer mean free path and are able to arrive at the substrate surface with higher energy and mobility, allowing for more dense film growth.

N_2 flow rate is another key parameter governing film growth. The ratio of N_2:Ar in the chamber during deposition will directly determine the stoichiometry of the deposited film, which has a significant impact on film quality [11]. The ideal ratio of N_2 to Ar gas leads to a 1:1 balance between nitrogen and niobium deposited on the substrate, allowing for stoichiometric grains of NbN to form. Substrate temperature and bias determine the adatom mobility of material which arrives at the substrate [9]. For higher temperatures and bias, the arriving Nb and N atoms have more energy to settle into favorable states, allowing for dense films with reduced impurities and void structures. Certain temperatures and biases, however, have been shown to promote growth of unwanted phases of NbN such as the hexagonal δ' and β phases [12].

Overall, developing a sputtering recipe for high-quality NbN is a multi-dimensional optimization problem. In this project, we are interested in the sputtering of NbN using a room temperature substrate such that its potential applications include the fabrication of all-nitride Josephson junctions [3]. This designates N_2 flow rate and substrate bias as the two most important sputtering parameters to be adjusted, once target power density and Ar flow rate have been determined.

1.3 Substrate Material

In addition to sputtering parameters, the choice of substrate has also been shown to have a drastic effect on superconducting critical temperature for sputtered thin films [13]. Large lattice mismatches between substrate and film result in decreased T_c and polycrystalline film structure, while small lattice mismatches can result in maximal T_c and single-crystal structure of NbN. Additionally, substrate crystal structure can promote the growth of particular phases of NbN [13]. In some cases, rather than being forced to fabricate on a particular substrate, researchers will grow thin buffer layers of material to lattice-match to their particular thin film. Thin buffer layers have been shown to be an effective tool in promoting lattice-matching and improved T_c for NbN in particular [3, 12, 13].

Other factors can also influence the choice of substrate for a particular application, such as ease of fabrication and loss mechanisms. For microwave systems, for example, amorphous oxide substrates are particularly lossy and are a poor choice for microwave resonators [14]. We discuss this in greater detail in section 4.5. In some cases, particularly for DC characterizations such as resistivity, an insulating substrate may be best.

In this project, we elect to use high-resistivity silicon due to its low loss at microwave frequencies, low cost, accessibility and ease of integration with existing fabrication methods. Its relatively high lattice mismatch of 18% ($a_{\mathrm{NbN}} = 4.46$ Å vs. $a_{\mathrm{Si}} = 5.43$ Å) will reduce the superconducting critical temperature of deposited films and produce randomly-oriented polycrystalline grains, but should still allow for the optimization of a substrate-independent deposition process. We prepare films on 500 μm thick single-side polished undoped high resistivity silicon ($\rho > 10000$ Ω-cm) purchased from University wafer (item 3811). While no significant pre-processing of these wafers is required before film deposition (e.g. thermal oxide growth), we do ensure that they undergo an RCA clean before deposition (see section 3.6).

1.4 Film Characterization

Ultimately, the best characterizations of the quality of a superconducting film are measurements of T_c and, if applicable, measurements of the internal loss rate κ_i of an electric field inside the film at frequencies and temperatures of interest. While these cryogenic characterizations provide the most direct evaluation of film quality, they are expensive in both time and resources.

Luckily, it is possible to obtain good evaluations of film quality at room temperature, which in some cases are correlated directly with superconducting properties [15]. High quality NbN films typically have low room temperature resistivity, usually on the order of 100 $\mu\Omega$ cm, with lower resistivity films being of higher quality [1]. X-ray crystallography can provide information about the nanostructure of a film, including crystal orientation, size, and density. A 111-orientation corresponding to the superconducting δ-NbN phase, large grain size, and high film density are all correlated with high T_c [7]. Additionally, X-ray photoelectron spectroscopy can be used to determine the occurrence of impurities in the film, which will adversely affect T_c.

In this work, we conduct measurements of room temperature resistivity, X-ray crystallography, and X-ray photoelectron spectroscopy to evaluate film quality immediately following deposition. From these room temperature measurements, we identify a subset of films which display the best electronic and structural properties to be tested at cryogenic temperatures.

Cryogenic evaluation of the films consists of patterning resonators onto the NbN film using photolithography and then observing the resonator response as they are cooled to 4.2 K in a closed-cycle cryostat. When the temperature of the resonator is below the critical temperature of the NbN film, we expect to see resonsant dips in the transmission spectrum, corresponding to the resonant modes that can only exist when the film is in the superconducting state. Above T_c, the film returns to the normal state and the resonant modes disappear. While this is an approximate method of determining T_c, compared to a more thorough DC 4-point probe measurement, it allows for more rapid testing and is sensitive enough for the films sputtered in this work. This measurement scheme also allows us to determine the intrinsic quality factor, Q_i, of each mode by fitting the peak with the expected Lorentzian function. A higher Q_i value indicates a higher-quality film with low internal loss. Typical Q_i values for NbN microwave resonators at 4.2 K are about 1000, although Q_i can depend on the power of the signal used to measure the resonator.

2 Benefits to the SNF Community

Although commercial superconducting NbN films are available, the ability to reliably deposit high quality NbN films in a shared tool can be beneficial to many in the SNF community. This work will add to the material processing capabilities of SNF by:

- Creating an SOP in the Lesker2 to deposit high quality NbN films
- Providing a framework for developing and testing future sputtering recipes
- Expanding the ability to test high T_c superconductors in SNF at low cost
- Determining the most important metrics for evaluating NbN film quality at room temperature
- Building a repository of NbN film and sputtering parameters

3 Process Development

Standard room temperature characterizations of thin films of metal include profilometry, resistivity, X-ray diffraction (XRD), and X-ray photoelectron spectroscopy (XPS); all of which are explained below.

A few preliminary experiments were conducted prior to sputtering NbN in order to set some of the more basic sputtering parameters. First, thin films of pure Nb and Ti were deposited using the Kurt J Lesker 2

Sputter Deposition Tool (Lesker2) system in SNF, detailed in section 3.4. Resistivites and deposition rates were compared to the Lesker3 system at SLAC (operated by Don Gardner). These results were used to finalize a proper target power and gas flow pressure, and allowed us to compare the Lesker2 conditions with a working system. Next, a fine measurement of the N_2 preconditioning hysteresis curve was performed in the Lesker2 in order to accurately determine the ideal range for the N_2 flow rate, detailed in section 3.5.

Once the target power, gas flow pressure, and N_2 flow rate range have been calibrated, we began sputtering NbN and performing the room temperature characterizations.

3.1 Film Thickness and Resistivity Measurements

Since thin films of metal are not transparent, traditional ellipsometry measurements do not work. To measure film thickness, we draw a radial line across our wafer substrate prior to deposition using a permanent marker, shown in figure 2(a). After sputtering, the marker line can be easily lifted off using acetone and IPA, exposing the wafer underneath. The height difference between the wafer surface and metal film surface is measured using a surface profilometer, either the Alphastep 500 Profilometer in SNF or the Dektak XT-S Stylus Profiler in SNSF.

The Prometrix Resistivity Mapping System in SNF uses a four-point DC probe measurement scheme for determining resistivity, shown in figure 2(b). Four points touch down onto the film material; current is forced through the outer two probes, while voltage is measured across the two inner probes, figure 2(c). The Prometrix uses the constant spacing between each of the probes to report the sheet resistance in Ω/sq. Multiplying the sheet resistance by the thickness of the film gives the standard resistivity in Ω-m.

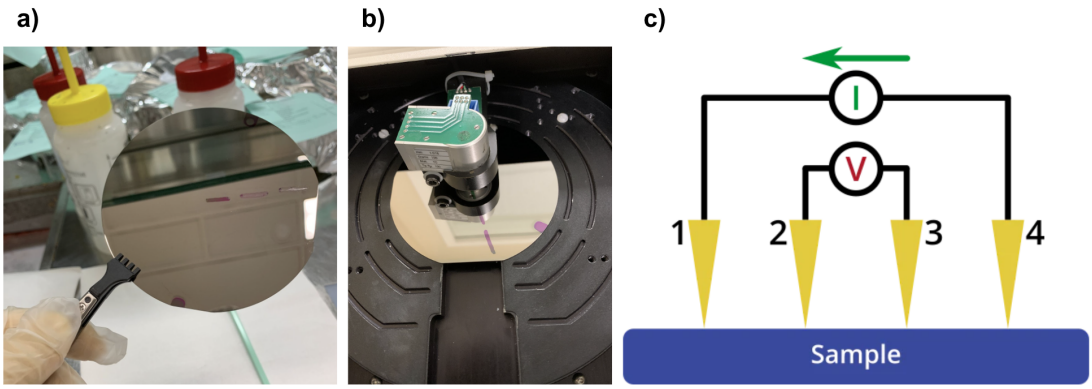

Figure 2: (a) A 4 inch wafer with a Ti thin film deposited via sputtering. After liftoff with solvents, the marks can be distinguished from the rest of the reflective metal. (b) A Ti sample loaded in the Prometrix for resistivity measurements. (c) A diagram of the four-point probe measurement apparatus.

3.2 XRD Measurements

X-ray diffraction measurements were performed using the PANalytical X'Pert 2 system located in the McCullough Building (Stanford University). Using a grazing incidence measurement, the x-ray incident angle can be swept asymmetrically. The location of the peaks in the reflected spectrum can be compared known NbN spectra from various databases. Fitting to the width of each peak allows one to calculate grain size, and determining the location of each allows one to determine the grain orientation.

Five NbN XRD spectra are plotted in figure 3 with the known NbN crystal orientations overlayed with black vertical lines. The 111-orientation corresponds to the superconducting δ-NbN phase. The peaks line up well with the known values of the NbN phases, with the exception of sample 2B, which was deposited with a 50 W rf substrate bias applied. The substrate bias shifts the peaks to smaller angles, which is consistent with previous literature [7].

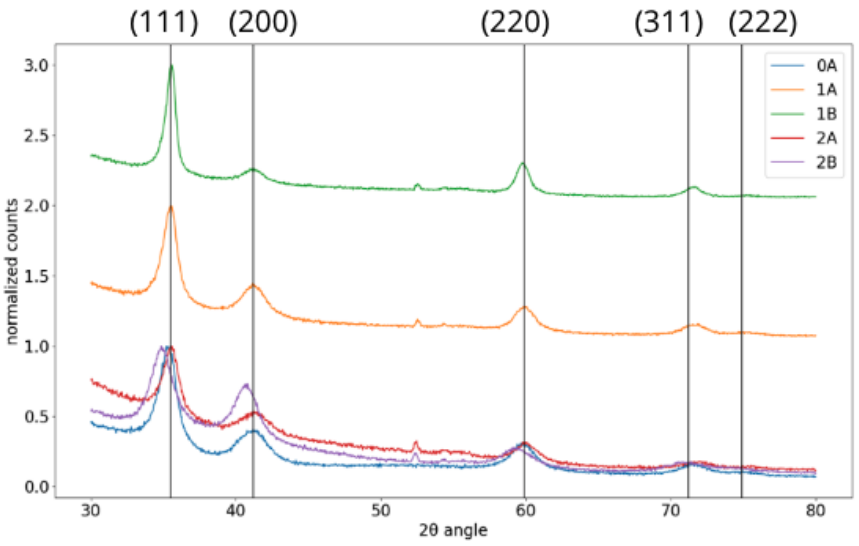

Figure 3: XRD spectra of calibrating NbN samples. Samples 0A, 2A, 2B were all deposited at a N_2 : Ar flow rate of 4%. Sample 1A was deposited at N_2 : Ar = 5%, 1B at N_2 : Ar = 10%.

3.3 XPS Measurements

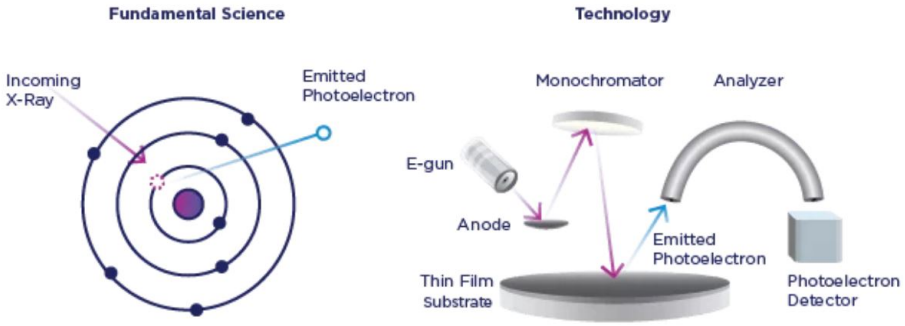

Figure 4: Fundamentals of XPS. Left, an incoming X-ray photon is absorbed by an atom and ejects a photoelectron from an inner shell in the process. Right, an X-ray beam is generated via the absorption of an electron beam by an anode. This X-ray beam is filtered and then focused on the surface of a sample. Emitted photoelectrons are collected by an analyzer where they are filtered according to their kinetic energy and measured by a detector. Figure from [16].

X-ray photoelectron spectroscopy (XPS) is a surface-sensitive spectroscopic technique used to evaluate the elemental composition of a sample. In XPS, an X-ray beam is generated and focused onto the surface of a sample where it penetrates several microns deep. As the beam penetrates into the sample, X-ray photons are absorbed by atoms and knock out inner shell electrons as depicted in Figure 4. These photoelectrons then leave the surface of the sample and are then collected by the analyzer, which sorts photoelectrons by their kinetic energy. The kinetic energy of each photoelectron is given by

$$\mathrm{KE} = E_\gamma - \mathrm{BE} - \phi^* \tag{1}$$

where E_γ is the energy of an X-ray photon, BE is the binding energy of the electron, and ϕ^* is the work function of the material (with adjustments to account for systematic effects from the instrument itself). Since E_γ and ϕ^* are known, and KE is measured by the instrument, XPS can determine the binding energy of each

detected photoelectron. This allows for identification of not only elemental composition but, in some cases, allows the inference of particular bonding states of each element [17]. XPS is considered surface-sensitive because these photoelectrons have a shallow escape depth of a few nanometers, but in-situ sputtering systems allow for the sample bulk to be measured as well.

In this project, we used the PHI VersaProbe III located in the McCullough Building to analyze the elemental composition of our deposited samples. Particularly, we were concerned that oxygen had contaminated certain films during deposition, resulting in heightened resistivity and poor film quality. In order to measure the bulk of the sample and eliminate surface oxidation, we sputtered each sample with an Ar^+ ion gun operated at 2kV, 1.5μA, and a 2mm x 2mm raster area for 8 minutes. This ion sputter time was determined by conducting a depth profile of a sample of NbN and finding a point at which the oxygen content of the sample reached a steady state. The sputter rate was assumed to be similar for all samples of NbN within the design of experiment.

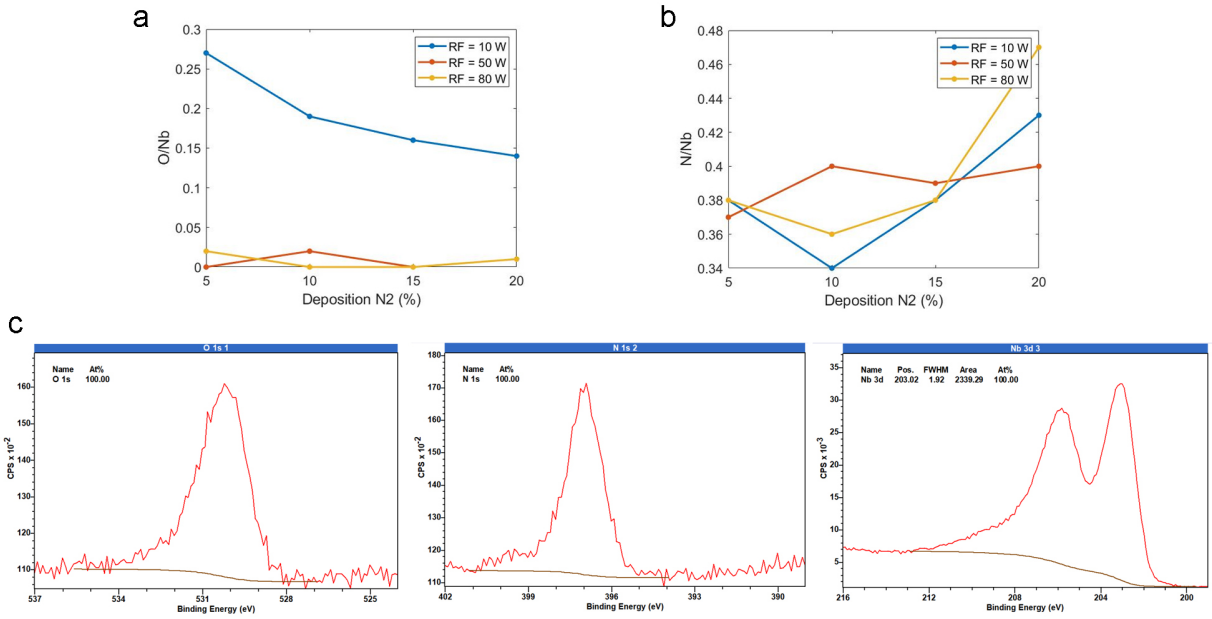

Figure 5: Results from XPS. (a) Ratio of oxygen to niobium content in samples, plotted across the ratio of N_2:Ar and for varying RF substrate bias. (b) Ratio of nitrogen to niobium content in samples, plotted across the ratio of N_2:Ar and for varying RF substrate bias. (c) Typical high-resolution spectra for oxygen, nitrogen, and niobium. In niobium, a more complex peak structure emerges due to different bonding states (nitrides, oxides, and unbonded metal) in the bulk of the sample.

The results of XPS analysis on samples of NbN are depicted in Figure 5. Notably, we find that the highest resistivity values across all samples of NbN can be attributed to high levels of oxygen content in the films. Particularly for low RF substrate bias, oxygen easily contaminates the film. The shape of the curve in Figure 5a indicates that the Ar gas line of the Lesker2 is a likely source of oxygen in the system – as N_2 gas flow is increased, Ar gas flow is decreased, and we see the oxygen content of the film decrease accordingly. This data indicates the existence of a critical RF bias above which oxygen impurities will be removed from the film.

The N/Nb ratios reported in Figure 5b seem to indicate that all sputtered films are extremely nitrogen deficient, since a stoichiometric film should yield N/Nb $\sim$ 1. This result, however, should be taken with caution. When sputtering with an argon ion beam, nitrogen is preferentially sputtered more quickly than niobium [18]. This leads to a nitrogen deficient surface and thus an artificially low N/Nb ratio. The authors in [18] found concentration gradients induced by Ar^+ sputtering to be as much as 50% in some cases. Thus, we do not believe the N/Nb ratios originating from XPS accurately identify the stoichiometry of the

deposited films.

There still exists more opportunity for film characterization using XPS. The niobium spectrum in Figure 5c shows evidence of multiple sub-peaks, which could be analyzed to determine bonding states of niobium in the film. Overall, however, due to the drastic preferential sputtering rates, we recommend other avenues for film stoichiometry analysis. The electron microprobe affiliated with the Stanford Microchemical Analysis Facility or a Time-of-Flight Secondary Ion Mass Spectrometer (ToF SIMS) could be used for more accurate, less biased measurements of elemental film composition in the future.

3.4 Nb and Ti Deposition

Niobium and titanium were deposited for 30 minutes using the preinstalled targets in the Lesker2. Depositions were performed at a target power of 100 W and 200 W. Sheet resistivity of the films was measured using the Prometrix in SNF (described in section 3.1) and compared to the bulk resistivity of Nb and Ti. In general, the resistivity of materials in thin films is higher than the bulk value.

Figure 6 shows the film resistivity and deposition rates of Nb and Ti. The black values from the SNF Lesker2 system are compared to those from the Lesker3 at SLAC (red values). Evidently the target power did not significantly affect the film resistivity. The film resistivity both in the Lesker2 and Lesker3 were quite higher than the bulk value, as expected, although the Lesker3 had lower values. This difference in resistivities can be attributed to the lower base chamber pressure before deposition (1×10^{-9} torr at SLAC vs. 5×10^{-8} torr at SNF), indicating less impurities in the SLAC system. The deposition rate in the Lesker2 was also around 2.25x smaller than that in the Lesker3, which can be attributed to the different cross-sectional areas of the targets (2 inch vs. 3 inch in radius). The 2.25x lower deposition rate allows for more impurities to enter the film during the deposition, leading to more impurities per unit thickness. As a result, when calculating the resistivities the Lesker3 films we find that they differ by a factor of roughly $\sqrt{2.25} = 1.5$. These results indicate the importance of starting sputtering depositions with as low a base chamber pressure as possible.

Film Resistivities (μΩ cm)

	Bulk	100 W Sample	200 W Sample
Titanium	42	*(62.3)* 99.6	*(61.3)* 96.9
Niobium	15.2	*(19.4)* 29.6	*(18.8)* 25.7

Deposition Rates & Film Thicknesses

Target Power (W)	Ti Thickness (nm)	Ti Dep Rate (nm/min)	Nb Thickness (nm)	Nb Dep Rate (nm/min)
100	89	*(6.1)* 2.97	90	*(7.8)* 3.0
200	168	*(12.4)* 5.60	156	(15.8) 5.2

Figure 6: Tables of the resistivity and deposition rates of Nb and Ti sputtered films. Red values are measured from the Lesker3 system by Don Gardner (SLAC), while black values were measured by us using the Lesker2 system at SNF.

3.5 N_2 Hysteresis Curve

Preconditioning the Nb target for depositing NbN requires first poisoning the Nb target with N_2 gas before setting the desired operating point [6]. This process involves slowly stepping the N_2 : Ar flow rate from 0% to 100% in fine increments with the shutters closed until the Nb target is fully saturated with N_2. When ramping down the N_2 flow rate, the trajectory of the target voltage will take a slightly different path, due to lingering effects of N_2 on the niobium target, creating the well-known hysteretic curve shown in figure 7(a).

An optimal N_2 flow rate occurs where this curve has the largest change, as it indicates a delicate balance between the amount of N_2 being deposited onto the niobium target and the substrate, hopefully leading to the deposition of stiochiometric NbN. As shown in figure 7(b), an optimal flow rate for the Lesker2 is around 4% to 10%. For the purposes of repeatability, the N_2 flow rate is always set after poisoning the Nb target by stepping along this hysteresis curve.

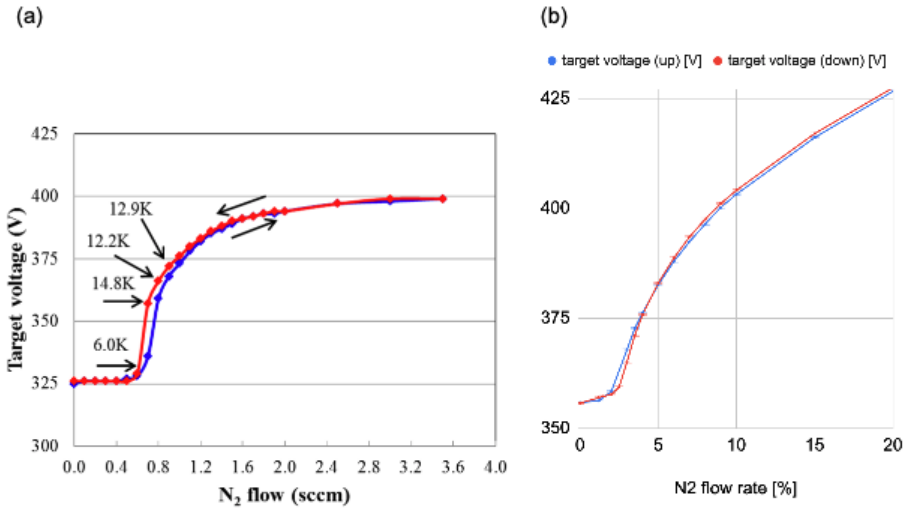

Figure 7: (a) N_2 hysteresis curve from [5]. (b) Measured N_2 curve in the Lesker2.

3.6 NbN Deposition

Once the preliminary work is finished, the deposition of NbN is quite straightforward and repeatable. The first step is to remove any trace organics, metals, or oxides on the wafers using a standard RCA clean. It is important to limit any potential sources of impurities during the deposition as this can significantly hinder the achievable T_c. To start off the deposition with a low chamber pressure, we either wait for the pressure to continue pumping down, or run a ten minute titanium burn-in to expel trace impurities and then wait for the pressure to settle down. We have found that around 5×10^{-8} Torr is an acceptable base chamber pressure. The sputtering parameters that we have fixed are the target power (100 W), and gas flow pressure (5 mTorr). The N_2 flow rate is always set by stepping along the hysteresis curve.

Twelve NbN samples were deposited in a design of experiment, discussed in section 5. Film thickness and resistivity measurements were performed for each NbN sample. XPS measurements were also performed on each NbN sample, but XRD measurements were performed only on a small subset of samples before the tool went offline due to a maintenance issue. A complete XRD characterization of all samples is worth while in the future. The most promising NbN samples were selected to pattern resonators and perform T_c and Q measurements, discussed in great detail in section 4.

We outline the complete recipe in our NbN Sputtering Standard Operating Procedure.

4 Resonator Fabrication and Measurement

Characterization of thin film NbN performance requires access to an environment below the expected critical temperature ($\leq$ 17 K). The traditional approach to measure T_c is the four-point probe method, which measures DC conductivity while avoiding contact resistance [19]. Other approaches include AC/DC susceptibility methods [20], the use of a SQUID magnetometer [21], and microwave resonator measurements [22–26]. The latter direction is pursued in this work, as it maximizes the number of films characterizable per cooldown while enabling estimation of the critical temperature and film quality through the resonance

characteristics. The presence of superconductivity, for instance, can be easily verified by measuring the red-shift of the resonant modes as a function of power and temperature (see section 4.4). Additionally, modes at temperatures above T_c would not be measurable at all due to the drastic increase in circuit resistance, which provides an accurate estimate of T_c. To perform this measurement on our films, we have developed a general procedure for patterning sputtered NbN. Our specific designs (planar microwave resonators) have utility in quantum information science [27–31], microwave kinetic inductance photon detectors (MKIDs) [32, 33], electro-optic devices [27], nano-electromechanical systems (NEMS) [30, 34, 35] and in fundamental studies of quasiparticle dynamics in superconductors [33, 36]. In the following subsections, we unpack the physics of this resonator and justify our design choices (sections 4.1, 4.2 and 4.3). Next, the full fabrication procedure is detailed in sections 4.5, 4.6 and 4.7. Our procedure requires only a single photolithography mask. The measurement protocol is then detailed in section 4.8 before presenting our results in section 5.1.

4.1 Introduction to On-Chip Microwave Resonators

The simplest electromagnetic resonator to fabricate and characterize is comprised of a single stripline waveguide. The fundamental mode has a resonance wavelength set by the quarter length of the waveguide:

$$\lambda_{res} = L/4 = c/n_{\text{eff}} f_{\text{res}} \tag{2}$$

In this expression, n_{eff} is the effective refractive index of the waveguide (NbN), c is the phase velocity of light in free space and f_{res} is the standing wave resonance frequency. By standard photolithography, patterning a resonator with length L on the order of 1000 μm is trivial. Such a device would have a resonance frequency of 1 - 10 GHz. At such microwave frequencies, a multitude of technologies are commercially available for measuring the resonances. Our approach is detailed in section 4.8. Although film characterization at room temperature, such as resistivity and film stress, requires wafer-scale films, cryogenic characterization becomes much more feasible with chip-scale films (e.g. 5 x 10 mm) due to limited space inside a cryostat. Further, a microwave frequency characterization requires the substrate to be bonded to a printed circuit board (PCB), which is attached to a copper plate to ensure proper thermalization. Our PCBs are too small to hold wafer pieces greater than 1 cm x 1 cm. An image of our resonator chip design is shown in figure 10 panel 3. Moving from wafer- to chip-scale has an effect on the patterning process, resonator design and CAD design layout. To maximize the utility of on-chip real estate, the resonator waveguide is curved into a meander (see section 4.2). On each chip, six meander resonators are patterned with different length such that they are frequency multiplexed. This is done to avoid overlapping of the resonant modes in frequency space. Each chip contains two pentagonal wire bond pads connected by a feedline, which enables characterization of all microwave resonators simultaneously via RF transmission measurements.

4.2 Coupling to a Microwave Resonator

A single meander quarter-wave resonator is depicted in figure 8a. The justification for using this resonator design over other possible designs is discussed in section 8.1. A resonator device is of no use unless it can be measured efficiently. To do this, the meander is inductively coupled to an on-chip feedline. Figure 8b shows a magnified view of the coupling region. The regions with NbN are white, while the orange regions are where NbN is etched to separate the waveguides from the surrounding ground plane. The orange is exposed during photolithography as described in section 4.6. For the quarter-wave resonance to exist, the waveguide is terminated by a short at one end ($Z = 0$) by connecting it to the superconducting ground plane. The ground plane also helps to shield the device from external magnetic flux noise via the Meissner effect. The inductive coupling strength, characterized by a "coupling" or "extrinsic" quality factor Q_e, depends on the substrate, the coupling length (500 μm in our case), and the spacing between the meander waveguide and the feeding transmission line (see figure 8b). While the total length L of the quarter-wave device determines its resonance frequency straightforwardly by equation 2 (see figure 8c), the Q_e must be determined by high frequency EM simulations (Sonnet). Using a 500 μm thick substrate of high resistivity Si ($\rho = 10000$ Ω-cm) and the resonator dimensions shown in figures 8a and b, the coupling is calculated from the simulated scattering parameter from port 1 to port 3, S_{31}, via $Q_e = \pi/2|S_{31}|^2$ [23]. The red asterisks in figure 8 denote the target Q_e and frequency of the six quarter wave resonators on our chip design. All

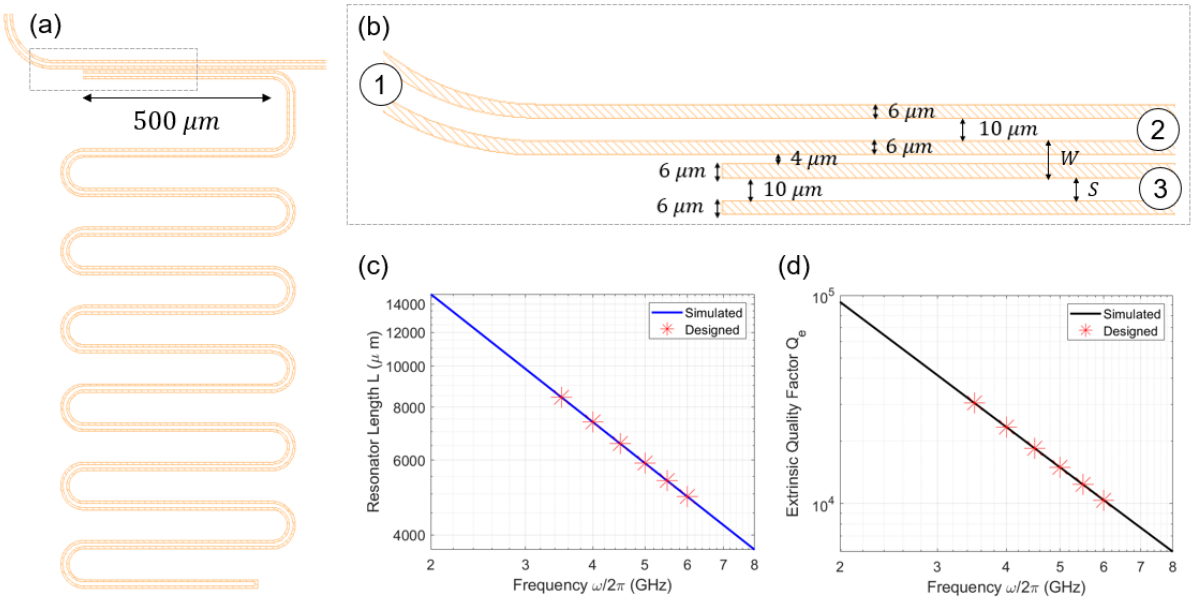

Figure 8: In (a), a sample meander waveguide microwave resonator is shown. Orange is indicates regions with no NbN, while white regions indicate areas with NbN. Figure (b) depicts a magnified view of the coupling region with ports labelled by 1, 2 and 3. The waveguide width of 10 μm and separation 16 μm together with the coupling length (500 μm) determine the coupling rate κ_e to the feedline. Figure (c) depicts the meander waveguide length L corresponding to the quarter-wave resonance frequency, while figure (d) illustrates the simulated extrinsic quality factor $Q_e = \omega_{res}/\kappa_e$ as a function of resonance frequency. The simulations were performed using Sonnet, while assuming a 500 μm thick substrate of high resistivity silicon (ρ = 10,000 Ω-cm) and $n_{eff} \sim 2.54$. The red asterisks on-plot indicate the chosen lengths for our on-chip resonators. The same coupler design was used for all resonators characterized in this report.

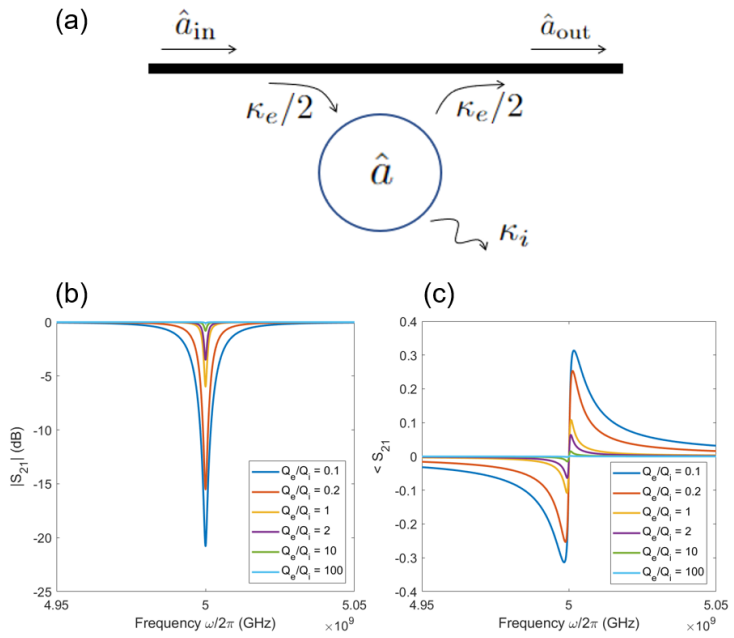

Figure 9: Figure (a) is a pictorial representation of a single microwave resonator with intracavity field $\hat{a}$ coupled to a transmission line by κ_e and coupled to intrinsic loss channels by κ_i. Figures (b) and (c) show the theoretical amplitude and phase spectrum of the transmitted signal S_{21} (equation 5) using $Q_e = 5000$, $Q_i = (500, 1000, 5000, 10000, 50000, 500000)$, and $\omega_{res}/2\pi = 5$ GHz.

resonators in this study had the same coupling length and waveguide spacings and only differed by their overall length L. Our objective was to be in the undercoupled regime $Q_i < Q_e$, where the total quality factor Q is primarily determined by the intrinsic quality factor Q_i (see section 4.3). This improves the accuracy of the fitted Q_i value. The intrinsic quality Q_i estimates the film quality while Q_e is purely determined by the inductive coupling strength. All resonators have in-plane dimensions much larger than the film thickness (are in the lumped-element regime), so the resonance frequency and coupling strength are independent of the film thickness. However, we note that a substantial correction to the coupling strength and resonance frequency may be necessary due to kinetic inductance nonlinearity in the film (see section 8.2).

4.3 Theory of Measurement for Microwave Resonators

The measurement of a microwave LC resonator can be described by lumped element circuit theory [37] or quantum optical input-output theory [38, 39]. Since our devices are primarily designed for quantum applications, we describe the microwave resonator response by recourse to input-output theory, where the equation of motion for the resonator cavity field is:

$$\dot{\hat{a}}(t) = -i\left(\omega_{\text{res}} - \frac{i\kappa}{2}\right)\hat{a}(t) + \sqrt{\kappa_e/2}\hat{a}_{\text{in}}(t) \tag{3}$$

which is subject to the symplectic boundary condition: $\hat{a}_{\text{out}} = \hat{a}_{\text{in}} - \sqrt{\kappa_e/2}\hat{a}$. In equation 3, the time evolution of the intrcavity field, $\hat{a}$, is determined by unitary evolution (first term) and damping with a total intensity decay rate κ (second term). At the same time, the cavity is being populated by a coherent tone $\hat{a}_{\text{in}}$ from the feedline, leading to a term $\sqrt{\kappa_e/2}\hat{a}_{\text{in}}$ characterized by an extrinsic coupling rate κ_e. The boundary condition expresses the output field $\hat{a}_{\text{out}}$ in terms of the input field $\hat{a}_{\text{in}}$. The resonator and feedline is shown abstractly in figure 9a. One can turn this differential equation into an algebraic one by moving into the

Fourier domain:

$$\hat{a}(\omega) = \int_{-\infty}^{+\infty} \hat{a}(t) e^{-i\omega t} dt \tag{4}$$

while making use of $F\{\dot{\hat{a}}\} = -i\omega\hat{a}(\omega)$. Thereafter, calculation of the transmission parameter is straightforward [25, 26]:

$$S_{21} \equiv \frac{\hat{a}_{\text{out}}(\omega)}{\hat{a}_{\text{in}}(\omega)} = 1 - e^{i\phi} \frac{\kappa_e/\kappa}{1 + 2i\Delta/\kappa} \tag{5}$$

where $\Delta = \omega - \omega_{\text{res}}$ is the detuning, and $\kappa_i = \kappa - \kappa_e$ is the intensity loss rate of the intracavity field that is not due to coupling to the feedline. The factor $e^{i\phi}$ is manually added to the second term to account for asymmetry in the resonance [40]. The intrinsic loss κ_i can arise due to a multiplicity of mechanisms, such as field loss into the substrate and loss due to coupling of the resonant electric field with defects/two level systems in the superconducting material or substrate. In our investigation, we are careful to compare samples with the same substrate to ensure that the measured intrinsic loss rate quantifies the quality of the superconducting film. The loss rate parameters can be related to the quality factor of the resonance by $\kappa = \omega_{\text{res}}/Q, \kappa_e = \omega_{\text{res}}/Q_e, \kappa_i = \omega_{\text{res}}/Q_i$, such that:

$$\frac{1}{Q} = \frac{1}{Q_i} + \frac{1}{Q_e} \tag{6}$$

We may extract the quality factors by fitting a measured resonance to the Lorentzian function $|S_{21}|^2$. In figure 9b and c we see the theoretical amplitude $|S_{21}|$ and phase $\angle S_{21}$ response of a microwave resonance at various Q_e/Q_i values ($Q_i = 5000$ is fixed). It is worth noting that the same S_{21} in equation 5 can be obtained by considering the impedances/admittances of a lumped element circuit comprised of a transmission line inductively coupled to an LC oscillator.

4.4 Verification of Superconductivity via S_{21} Measurements

The discussion in the previous section describes the measurement of a linear electromagnetic resonator via a transmission line. The T_c did not enter this discussion. Accurate determination of film quality (especially T_c) requires an understanding of superconductivity and the mechanisms which can affect the resonance frequency and lineshape. A superconductor consists of electron-electron pairs (Cooper pairs), bosonic states that traverse a superconducting material with zero DC resistance. In the absence of sufficient thermal excitation ($T \ll T_c$), the Cooper pairs accumulate in the quantum ground state. According to Bardeen–Cooper–Schrieffer (BCS) theory, the photon energy needed to break up a Cooper pair is given by $\hbar\omega_c = 2\Delta = 3.52 k_B T_c$ where Δ is the superconductor energy gap [33, 36]. This energy gap is conceptually analogous to the gap in semiconductors that must be overcome to generate an electron-hole pair. In a superconductor, 2Δ is the binding energy of a Cooper pair. By the BCS formula, an $\omega_c = 166.5$ GHz photon is required to break apart a Cooper pair in a superconductor with $T_c = 8$ K. A sufficient flux of photons with this energy would force the material out of the superconducting state. This frequency is much higher than the frequency of our resonator photons (< 10 GHz). However, just as superconductors share the concept of an energy gap with semiconductors, they also have a band structure comprised of many possible Cooper pair states. It has been shown [22, 36] that the power dissipated by a microwave signal (with $\omega < \omega_c$) can cause the quasiparticles in a superconducting to switch between states. This effect manifests in the measured microwave resonator spectrum. At low readout powers, only a single state is populated. As the readout power is increased the resonance curve distorts (it nonlinearly redshifts) [22, 36]. The effective temperature of the quasiparticle system rises until a balance is reached between the rate at which microwave energy is dissipated in the resonator, and the rate at which energy is transferred from the quasiparticle system to the phonon system of the substrate [22, 36]. At high readout powers, three states exist, two of which are stable, and the resonance curve shows hysteresis [22, 36]. The resonance in this situation has infinite slope at the bistability frequency. Observation of redshift and bistability in our resonators would strongly hint at the presence of superconductivity. This approach would also be useful for locating the resonance peaks in

a given transmission spectrum that may contain spurious non-superconducting peaks (e.g. due to wirebond resonances). To avoid the hassle of nonlinear peak fitting, Lorentzian fitting should be performed on data acquired while at low temperature and power where linearity is sustained. Thereafter, the temperature inside the cryostat (or microwave signal power) could be gradually ramped and the transmission spectrum retaken. Beyond the critical temperature T_c (or critical power P_c), all Cooper pairs break and the increased impedance of the sample indicates transition out of the superconducting state. Such a measurement would set a lower bound on the film T_c (or P_c).

4.5 Resonator Fabrication Considerations: Substrate Type and Dicing

The superconductivity of an NbN film can be characterized so long as the substrate is a sufficiently good insulator. At first, silicon dioxide may appear to be a good option. However, it is known [14] that microwave resonators on silicon dioxide have low quality factor and would therefore be difficult to measure. The electric field couples to two level systems (vacancy sites) in the oxide. This mechanism serves as a loss channel for the resonator, and is present for many amorphous materials/glasses. We wish to remove all contributions to the intrinsic loss that are not due to the quality of the NbN film. As such, low loss high resistivity silicon is the substrate that we employ.
To dice our NbN-on-high resistivity Si wafers into 5 x 10 mm chips for resonator fabrication and measurement, we first dehydrate the wafer at 180 C for 2 minutes, then spincoat the wafer with protective SPR-220 resist (2000 rpm, 2000 ramp, 40s) and prebake at 110 C for 120 s. For dicing we have employed a DISCO wafer saw (SNF) with a standard hub blade at a cutting speed of 2 mm/s and a blade height of 300 μm. Partially diced chips can then be removed from the dicing tape by tweezers and subsequently cleaned using acetone and isopropyl alcohol (30 s each).We have found that dicing through the full 500 μm wafer causes the wafer pieces to eject from the dicing tape.

4.6 Microwave Resonator Fabrication Procedure

In this section we outline the procedure for fabricating microscale structures on NbN. We verify the effectiveness of this procedure for both high resistivity silicon and silicon dioxide substrates. The latter samples were obtained while comparing the lesker2 and lesker 3 performances. A similar procedure could also be used for patterning tantalum, NbTiN or other nitride films. The procedure is fully described in steps by figure 10.

1. **Chip Cleaning:** After NbN deposition and dicing, be sure sure that chip has been cleaned of SPR-220 dicing resist. Perform a 30 s acetone and ipa rinse.

2. **Spin-coat:** Dehydrate the chip on a hotplate at 180 C for 2 min. Spincoat the chip with SPR-3612 positive resist at 5500 rpm, 1500 rpm/s, 40 s. Use 2-3 pipette drops per chip. Then prebake on a hotplate at 90 C for 1 minute.

3. **Photolithography:** Using the desired dxf file for the appropriate chip size, expose the chip using the Heidelberg MLA150 (SNF) with a uniform dose of 100 mJ/cm^2. Before exposure, check the chip backside for resist and ensure that the chip is aligned with the Heidelberg stage axes. Heidelberg can easily pattern our minimal feature size of 4 μm.

4. **Development:** After the exposure, develop the resist in MF-26A for 20 s followed by 10 s of DI water. The pattern should now be visible by eye. Use a microscope to do an exposure check. Make sure to view the chip edges and the smallest gap feature to verify a successful exposure and develop. One may submerge the chip in MF-26A for additional time if needed. The development is not time sensitive.

5. **Plasma RIE:** Perform a chamber clean of the Oxford RIE (SNSF) using 50 sccm O_2 and 200 W discharge power for 5 minutes. Then precondition the chamber using the NbN recipe (LINQS_Ti_etch_01), which is 20 sccm CF_4 and 2 sccm O_2 at 210 W power for 2 minutes. Open the chamber to deposit your sample. Do not leave the chamber open and or vented for long, as this increases contamination and makes it more difficult to achieve process pressure of 100 mTorr after re-initiating the pumpdown. Perform the NbN etch. The only variable to alter is the etch time, which depends on the NbN sample

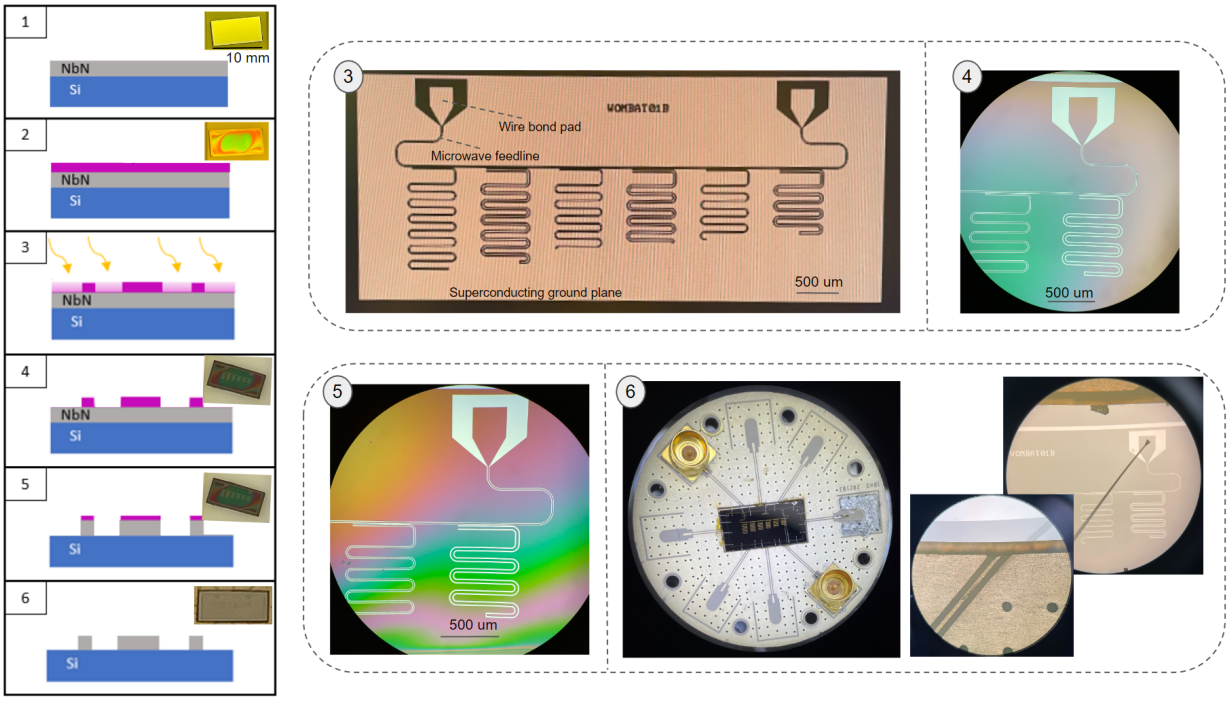

Figure 10: The procedure for patterning and wire bonding microwave resonators is shown. Panel 1 depicts a diced 5 x 10 mm high resistivity silicon chip with an NbN film. The chip is spin-coated with SPR-3612 positive resist (5500 rpm, 1500 ramp, 40 s). Panel 2 shows a resist covered chip. The chip is then exposed by a 375 nm photon beam (Heidelberg MLA150) with a uniform dose of 100 mJ/cm^2. Panel 3 shows the CAD file utilized for all of our 5 x 10 mm chips in this study, with exposed regions in black. After exposure, the photoresist is developed using MF-26A for 20 s and checked under an optical microscope (see panel 4). Next, the pattern is transferred to the NbN film through a plasma reactive ion etch (Oxford Plasma Pro 80 Reactive Ion Etcher RIE), which removes NbN at 1 nm/s (see panel 5). Lastly, the remaining resist is stripped by placing the chip in an N-Methyl-2-pyrrolidone (NMP) bath for 90 min. The chip is mounted to a printed circuit board (PCB) with diluted GE varnish and wirebonded to this PCB (with a West Bond 7476E Wedge-Wedge Wire Bonder) for cryogenic measurements, as shown in panel 6.

thickness. We measured the NbN etch rate to be 1 nm/s (see section 4.7). The thickness of the NbN film should be known before initiating the resonator fabrication procedure (see liftoff method in section 3.1). An overetch by roughly 30 nm (30 seconds) should be employed to ensure that the etch gets through the NbN. We have found that the etch profile is highly directional and that there is little risk associated with an overetch (see section 4.7). We have also found that the photomask is thick enough to survive at least a 4 minute long etch.

6. **Resist Strip:** After the etch, verify that all of the NbN has been removed. This can be done via optical microscopy by comparing with a previous sample positioned in the same field of view. The etch rate of 1 nm/s is quite consistent, so the etch check is typically not necessary. Once confident in the etch, place the chip in an NMP solution for 90 min, then rinse with acetone and IPA (30 s each).

7. **Wire Bonding:** Glue the chip to a PCB using GE varnish. Employ the West Bond 7476E Wedge-Wedge Wire Bonder (SNSF) to attach Al wires between the PCB ground plane and the chip ground plane and between the wirebond pads and the PCB traces. Aim for short wirebonds and use many wirebonds between the ground planes to improve the transmission measurement signal.

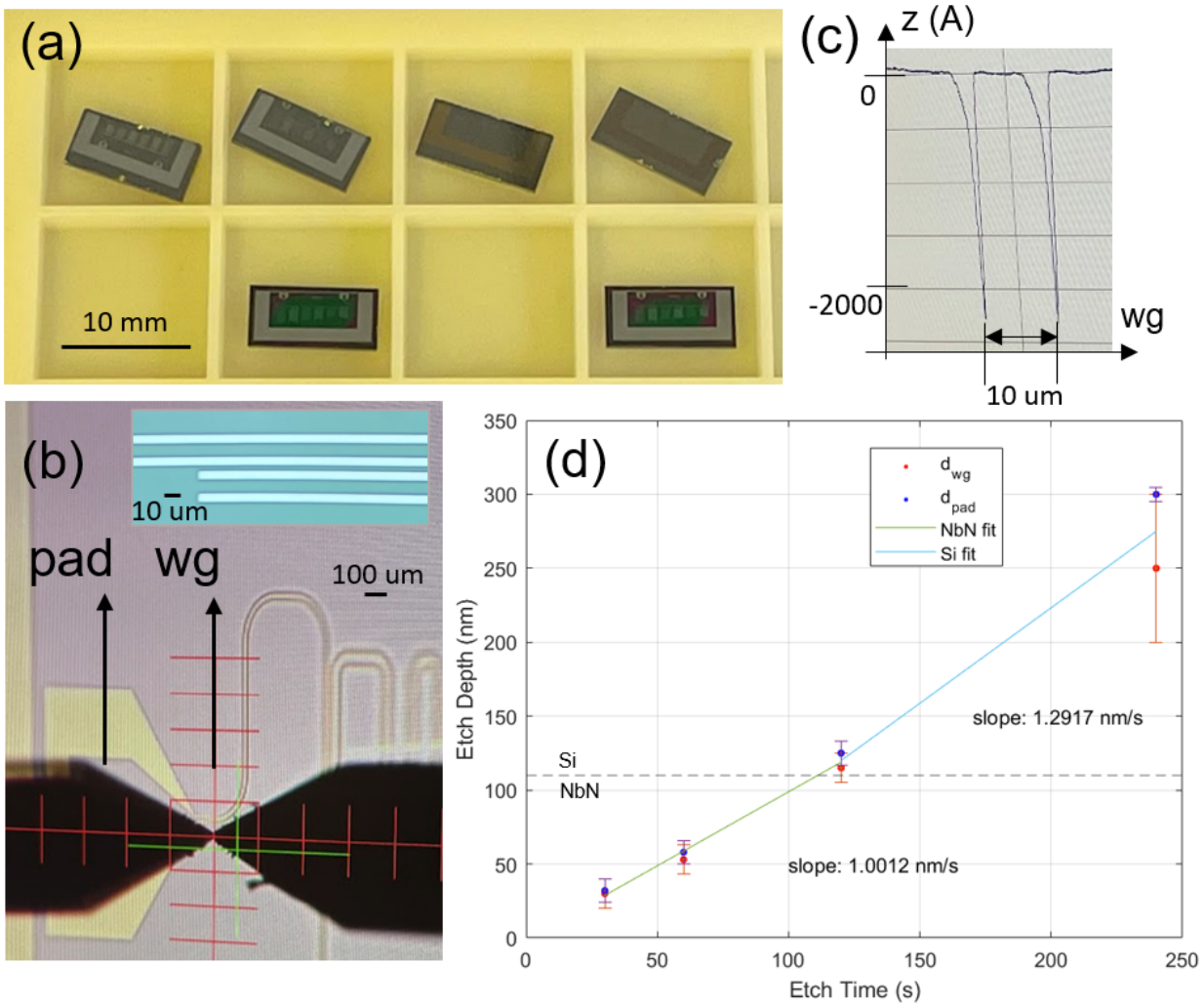

Figure 11: (a) The chips used for the RIE etch test are shown in the top row. They have been stripped of resist with NMP for profilometer measurements. From left to right the etch time was 4 min, 2 min, 1 min and 30s, respectively. The difference in the etch depth is reflected by the pattern contrast with respect to surrounding unetched NbN. The two chips in the second row are example chips with resist after etching fully through the NbN (before NMP bath), which demonstrates sufficient selectivity of NbN over resist. (b) An example profilometry measurement after an NbN etch and resist strip. Measurements were taken across the waveguide (wg) and the bond pad (pad). The inset optical microscope image shows a clearly resolved 4 μm gap (no resist), the smallest gap present in our design. The measurement result of the profilometery measurement in (b) along the wg direction is depicted in (c). This plot shows the steep etch profile achieved by a 4 minute anisotropic CF4 dry etch with SPR-3612 mask. The etch depth of 250 nm implies that the 110 nm NbN film has been etched through. The etch depth of each test chip is shown as a function of etch time in (d). Using 110 nm as the NbN thickness measured before patterning, we linearly fit the Si and NbN regions of the plot to infer a Si etch rate of 1.29 nm/s and NbN etch rate of 1 nm/s.

4.7 NbN Etch Test

For transmission line or nanowire fabrication, it is important that the etch is directional to produce nearly vertical sidewalls. It is also important to know the etch rate to ensure that the NbN is etched entirely through (to avoid a short in the circuit). At the same time, one wishes to avoid over etching such that the photomask is removed or the waveguide wire is undercut. To transfer the high aspect ratio meandered co-planar resonator pattern onto the NbN film, we employ reactive ion etching using an Oxford Plasma Pro 80 system (SNSF). The main etching gas is CF_4, while O_2 gas is also utilized in small quantities to control the etching rate ratio and selectivity with respect to the mask. This recipe has been utilized previously to create high aspect ratio structures, such as superconducting nanowires with vertical sidewalls [41–43]. The etch of NbN with CF_4 is governed by the reaction equation [43]:

$$CF_4 + 2NbN \rightarrow 2NbF_3 + N_2 + 2CF \tag{7}$$

For the etch test, we performed resonator fabrication on four 5 x 10 mm NbN on high-resistivity Si chips with 110 nm NbN thickness. The four chips with photomasks still on were etched with different etch times. Because of this, only one chip was in the Oxford etch chamber at a time. Before etching each of the four chips, the reaction chamber was cleaned by flowing 50 sccm O_2 with 200 W discharge power at 100 mTorr for 5 minutes. The chamber was then conditioned by running the NbN etch recipe for 2 minutes, where CF_4 and O_2 gases are flown in at 20 sccm and 2 sccm, respectively, with 210 W power (DC bias 360 V) at 100 mTorr ("LINQS_Ti_etch_01"). Thereafter, the sample was placed into the chamber. The four chips of identical initial NbN thickness were etched for 4 minutes, 2 minutes, 1 minute and 30 seconds. Thereafter, the resist was removed by NMP and the step height was measure using the Dektak XT-S Stylus Profiler (SNSF). The four chips after profilometry are shown in the first row of figure 11a. In this image there are also two chips in the second row, which are representative of chips with resist still on after an etch fully through the NbN. This demonstrates sufficient selectivity of NbN over resist. Profilometry was performed across two distinct regions of etch test chip: 1) across the gap near the pentagonal wirebond pad (pad), and 2) over the feedline waveguide (wg) as seen in see figure 11b. The inset shows an optical microscope image of a resolved 4 μm gap after photolithography and etching. The etch profile and etch rate can be extracted from a profilometry measurement, such as the one in figure 11(c). This example data was acquired by moving the stylus across the 4 min chip over the wg. The profile depicts a trench just under 250 nm deep (d_{wg}), indicating that the NbN was etched through. The etch profile is quite vertical and the waveguide width of 10 μm appears to have been properly transferred onto the NbN substrate. Since the etch is quite directional, it may be sensible to extend the etch time such that the waveguide edge is more vertical and the 4 um gap resolves better. Overall, we find that there is very little risk of undercut or exceeding the photomask. Additional investigation via angled scanning electron microscopy (SEM) may reveal better information regarding the etch profile. The etch is expected to be quite anisotropic since the plasma is generated under vacuo by an RF field, which then directs ions down towards the substrate with high energy to react with NbN then desorb as volatile products as described by equation 7. Figure 11d shows the maximum etch depth along the wg and pad directions (d_{wg} and d_{pad}) for the four chips as a function of etch time. The NbN thickness of 110 nm is indicated on-plot by a dashed line. Fitting the data below this line (NbN) and above this line (Si) yields an etch rate of 1.0012 nm/s for NbN and 1.2917 nm/s for high resistivity Si (selectivity 0.77).

4.8 Packaging and Cryogenic Measurement

Meander resonators can be excited and measured via an RF tone by wire bonding to the pentagon-shaped pads (see figure 10 panel 3). After fabrication, the 5 x 10 mm chips (with six resonators each) are glued to PCBs using GE varnish (see figure 4.6 panel 6). The pads on either end of the feedline are then wirebonded to a PCB signal trace (coplanar waveguide) which are soldered to SMP connectors, as shown in figure 12a. The NbN ground plane is wirebonded to the PCB ground plane. To ensure a uniformly distributed electric field in the ground plane, we employ many wirebonds connecting different regions of the ground plane to the PCB ground. We aim for the shortest wirebonds possible to push wirebond resonances to high frequencies where they are less likely be present near the frequencies of our resonators. After wire bonding, the PCB is placed on a copper plate contacting the cryostat floor to ensure proper thermalization. Cables then connect the SMP connectors to RF ports on the inside of the cryostat. After pumpdown and cooldown to base (1e-8

Torr and 4.2 K), we use SMA cables to connect a vector network analyzer (VNA) to the RF ports on the outside of the cryostat to measure S_{21} for each chip [25, 26]. Our radiation-shielded liquid He cryostation (Montana Instruments Cryostation s200) only has six ports, which allows for the characterization of three chips (films) per cooldown, for a total of 18 resonators. The signal path is highlighted in figure 12a. The signal outputted by VNA port 1 passes through the cryostat RF port onto the PCB (trace is shown in red) and onto the chip via Al wirebonds. It travels from pad to pad through the on-chip feedline and then exits the cryostat in a similar manner through port 2. The VNA measures the signal at port 2 and compares it to the outputting power at port 1, thereby recording the S_{21} parameter.

Figure 12b depicts the transmitted signal as a function at various temperatures (with fixed power -20 dBm). One mode is visible. Figure 12c shows the transmission spectrum for resonator of higher frequency on the same chip as a function of power (with a fixed temperature of 4.2 K). After changing each power or temperature, the sample was given up to 5 minutes to thermalize/stabilize. We can be confident that the modes are superconducting since they exhibit all of the properties discussed in section 4.4. There is a maximally linear Lorentzian resonance at low temperature. As the power/temperature increase, we observe a nonlinear redshift in the resonance peak and at sufficiently high power, there is a bistability, as indicated by the infinite resonance slope at (-20 dBm, 7.5 K) and at (4 dBm, 4.2 K). Once the temperature and power reached 8 K and 6 dBm, respectively, the resonances vanish and the transmission spectrum flattens out. This indicates that the film is no longer superconducting and incoming waves cannot propagate on-chip from port 1 cannot reach port 2. A low power (-20 dBm) was used for the temperature sweep to ensure that the resonator exits the superconducting state solely due to temperature increase to determine T_c. Likewise, the power sweep was done at low temperature to best estimate the critical power. The data in figures 12b and c was acquired from a 80 nm thick NbN on 1 μm thick oxide sample (2B), however similar citical temperatures and powers were gathered for our 60 nm NbN on 500μm high resistivity Si samples (see section 5.1.

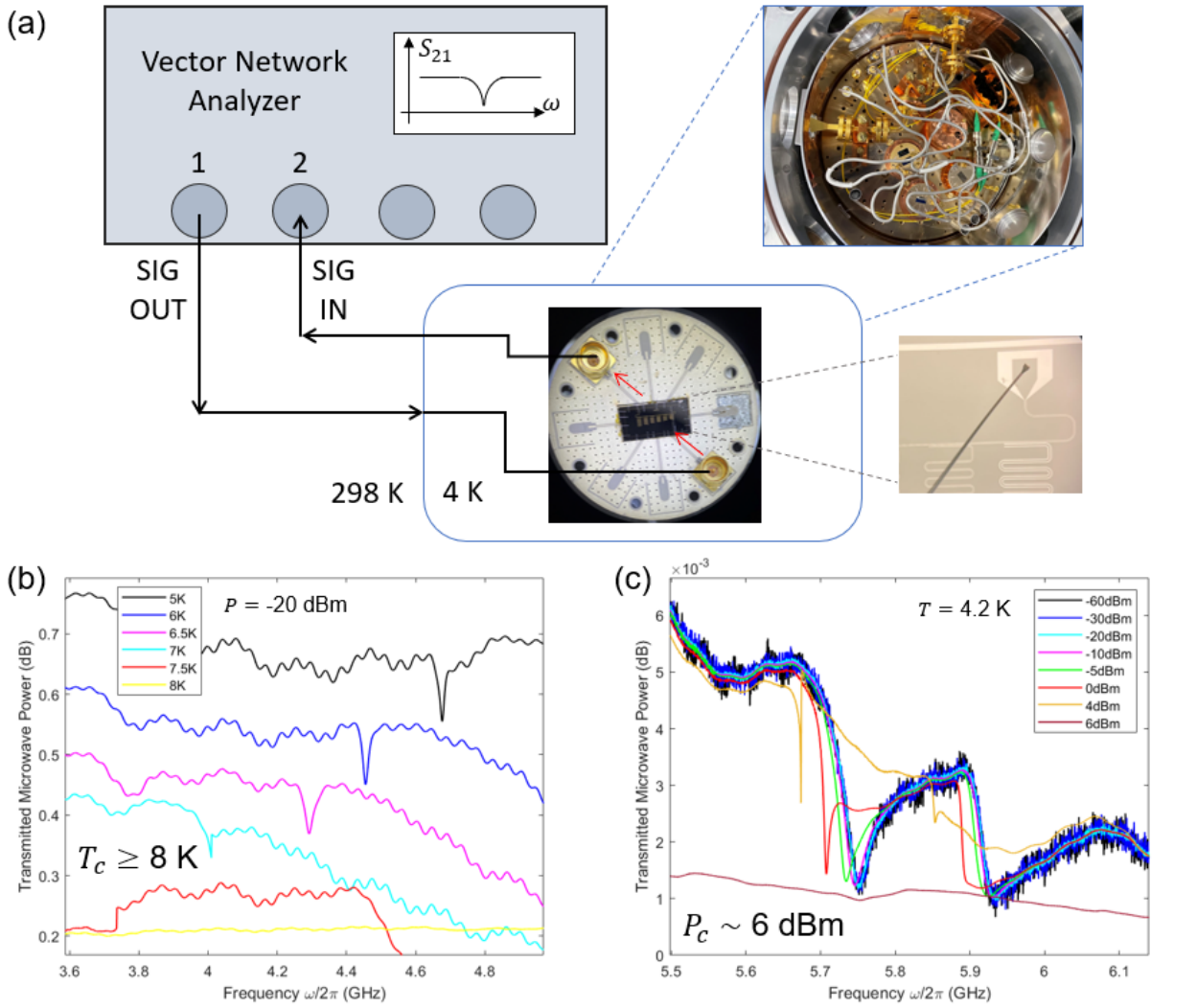

Figure 12: (a) A schematic representation of our cryogenic RF frequency measurement setup. A vector network analyzer (VNA) generates an RF signal at port 1 near the resonance frequency, which makes its way into the cryostat, onto the PCB through the SMP connectors and onto the chip via an Al wire bond. Red arrows indicate the signal path along the PCB traces. The signal propagates on-chip along the feedline and interacts with each resonator before travelling off-chip, out of the cryostat and into the VNA port 2. A picture of the cryostat interior before cooldown is shown. By sweeping the RF tone frequency across resonance, one can measure the transmission spectrum, which contains resonances at frequencies defined by each on-chip resonator length. The power of the RF tone and or the temperature of the cryostat may be changed and the transmission spectrum re-acquired. Figure (b) depicts the transmission spectrum containing one resonant mode as a function of temperature while drive power is fixed at -20 dBm. The critical temperature above which the mode disappears is roughly 8 K. Likewise, figure (c) depicts the power spectrum as a function of drive power as the temperature is held at 4.2 K. The critical power at which the film heats out of the superconducting state is 6 dBm. The spectra in (b) and (c) were acquired using a NbN-on-oxide film (sample 2B from section 3.2), which is clearly superconducting.

5 Design of Experiment Results

The two parameters deemed most critical for depositing high T_c NbN films were N_2 flow rate and substrate bias. We decided to test four N_2 flow rate points at 5%, 10%. 15%, and 20%. We expected to see a strong

window for stiochiometric NbN near 5% to 10% N_2 flow rate. Three RF substrate bias values were applied: 10 W, 50 W, and 80 W. We expected larger substrate bias of around 50 W to be effective in removing impurities during the sputtering process but did not know what to expect at very large bias values ($\sim$ 80 W).

We randomized the order in which we deposited each sample to limit any systematic correlations and deposited all of them over the course of two days, without another user using the Lesker2 system in between. This gives us good reason to believe the data trends come soley from the dynamics of the sputtering process. All the twelve samples are shown in figure 13.

Sample ID	N2 flow rate [%]	Substrate bias [W]
1	5	10
2	15	10
3	5	50
4	20	80
5	15	80
6	10	50
7	15	50
8	20	10
9	10	80
10	5	80
11	20	50
12	10	10

Figure 13: Table for all the design of experiment samples. Samples were deposited in increasing ID order. The three samples in yellow were used to pattern resonators and in cryogenic measurements.

The resistivity and film thickness of all the twelve samples can be seen in figure 14. All the sample values are written in red and the samples chosen for resonator fabrication are highlighted in yellow. Three samples from this DOE were chosen (shown in yellow in figure 13) for cryogenic measurements due to their low room temperature resistivity and relatively similar film thickness values of $\sim$60 nm. Three samples of NbN on oxide were also measured.

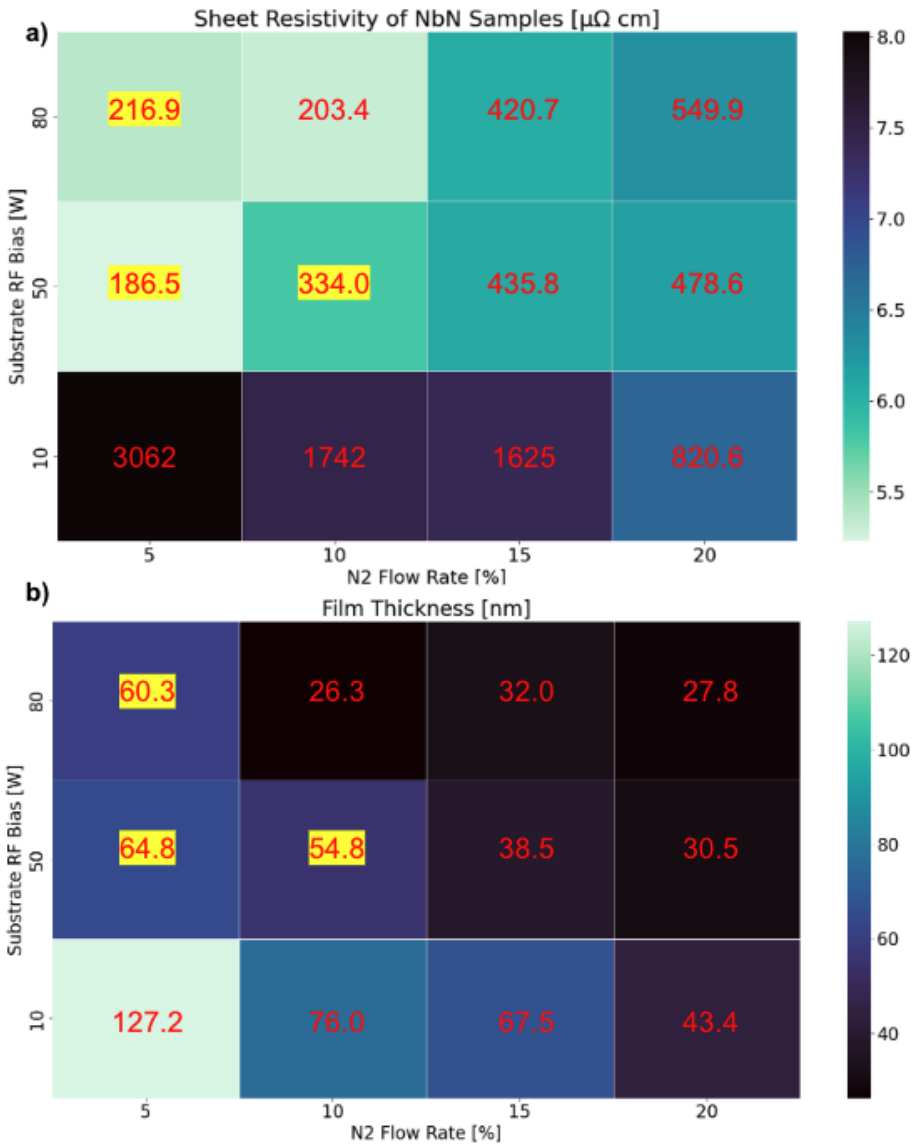

Figure 14: (a) resistivity (b) film thickness after 30 min deposition

Evidently the ideal window for low room temperature resistivity occurs for 5% to 10% N_2 flow rate and large substrate bias, as expected.

5.1 Cryogenic Microwave Resonator Measurements

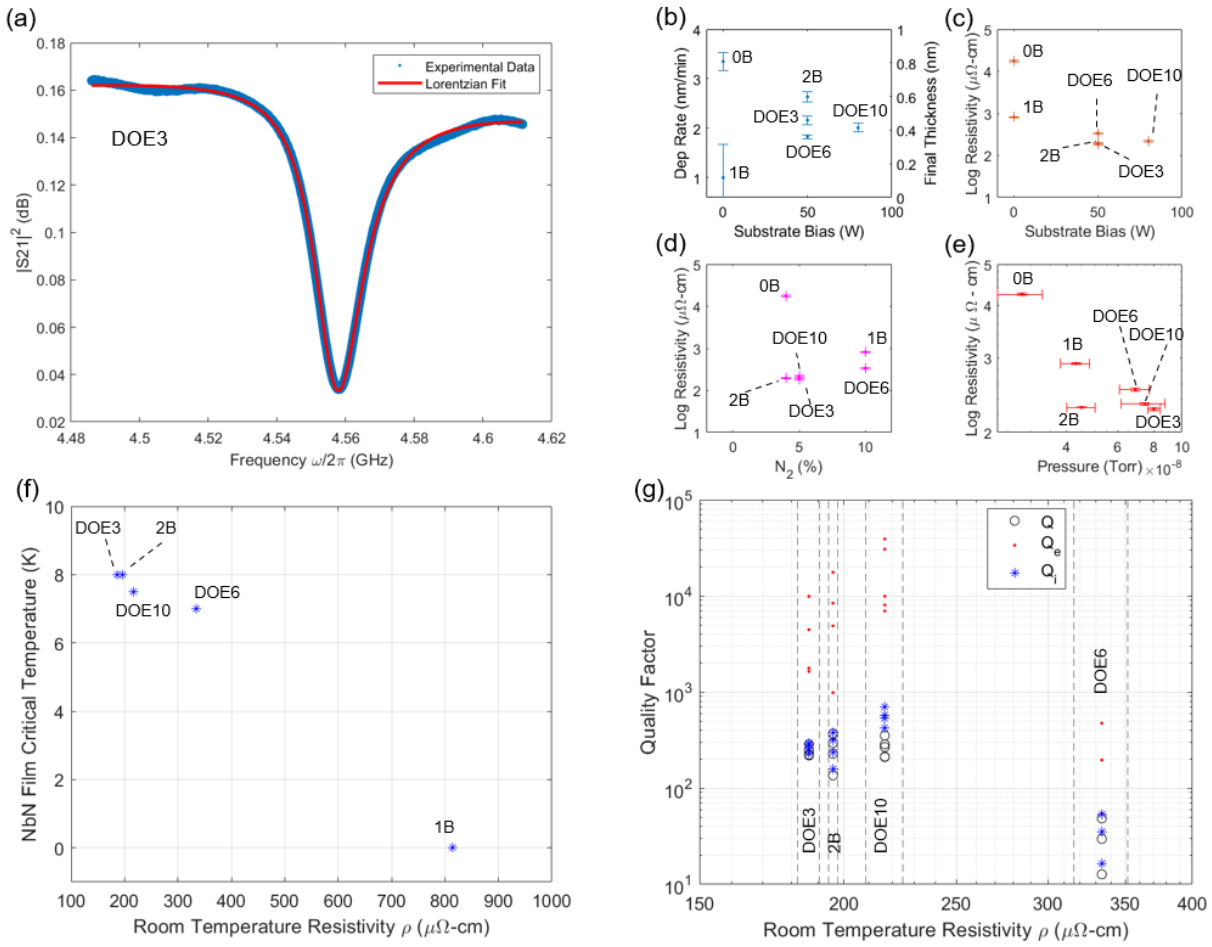

Figure 15: Three NbN on high resistivity Si (DOE3, DOE6 and DOE10) and three NbN on 1 μm oxide on Si chips (0B, 1B, 2B) were patterned using the same CAD file and measured using the technique described in section 4.8. Figure (a) shows a representative transmission spectrum measurement of a superconducting microwave resonator (DOE3) in blue acquired at 4.2 K with -20 dBm drive power. The spectrum is theoretically fitted (red) using equation 5. Figures (b) and (c) show the deposition rate and resistivity of the six samples as a function of substrate bias, respectively. The room temperature resistivity as a function of N2:Ar percentage and base pressure of Lesker2 is depicted in (d) and (e), respectively. The four lowest resistivity chips were superconducting with their corresponding critical temperatures plotted in (f). The 1B and 0B samples were not superconducting. The transmission spectrum of all resonators on each superconducting chip were measured at 4.2 K and -20 dBm drive power and theoretically fit to extract the quality factors, which are plotted in (g). The dashed error lines quantify the uncertainty in the resistivity across the wafer that the chip sample came from.

Figure 15 is a summary of the results of our initial NbN on oxide fabrication run (0B, 1B and 2B) and the DOE study (DOE3, DOE6 and DOE10). All films were deposited with 100 W target power, 5 mTorr Ar pressure (where hysteresis slope is maximized), and the deposition time was 30 minutes for all samples. Three NbN on high resistivity Si and three NbN on 1 μm oxide on Si chips were patterned using the same CAD file and measured using the technique described in section 4.8. Each chip contained six resonators. Figure 15a is a representative transmission spectrum measurement of a superconducting microwave resonator on chip DOE3 (blue) acquired at 4.2 K with -20 dBm drive power. this spectrum is theoretically fitted (red) using

equation 5, yielding parameters of $\omega_{res}/2\pi = 4.56$ GHz, $Q = 261$, $Q_e = 962$, and $Q_i = 359$. Resonance peaks were identified in the transmission spectra by confirming the presence of redshifting as a function of signal power (see section 4.4). Figures 15b and c show the deposition rate and room temperature resistivity of the six samples as a function of substrate bias, respectively. Higher substrate bias leads to lower deposition rate. However, we find that the errorbars, indicative of the non-uniformity of the film thickness across the original wafer, are smaller for larger substrate biases. We also find that samples acquired at the same substrate bias for the same sputtering time (30 minutes) have roughly consistent deposition rates if the substrate bias is large. Large substrate bias leads to better control over deposition rate. We can also can notice that the higher resistivity samples were acquired with larger substrate biases, since bias drives away oxygen impurities in the chamber, preventing them from adsorbing to the film during the deposition (see section 3.3). The room temperature resistivity as a function of N2:Ar percentage and base pressure of Lesker2 is depicted in figures 15d and e, respectively. The optimal N2 percentage appears to be 5- 10 % as in [25], however further confirmation of the Nb/N ratio is needed from addition XPS, electron probe, or mass spectrometry measurements. Figure 15e suggests that the film resistivity is independent of base pressure so long as it is below 10^{-7} Torr. Though not reflected in this plot, we have found that pressures far above the 1e-8 Torr value lead to very high film resistivity. Figure 15e shows the pressure right before the deposition (not during). Note that this pressure was read off the Lesker2 software without throttling the pump (so it may not be entirely accurate). During the transmission measurement of each chip, it was found that all three DOE (high resistivity Si) chips were superconducting and only one of the oxide chips was. These were the four lowest resistivity chips. We have no reason to argue that the substrate effects T_c, only that it effects Q_i. The main predictor of superconductivity of a given film is resistivity. The superconducting sample resistivities along with their corresponding critical temperatures are plotted in figure 15f. Critical temperature was measured by performing a temperature ramp transmission measurement as shown in figure 12b. We find that a resistivity of 800 $\mu\Omega$-cm is insufficient for superconductivity (Chip 1B), while 334 $\mu\Omega$-cm (Chip DOE6) is. Resistivity is a simple room temperature measurement that one can perform in SNF right after sputtering a film in Lesker2 to determine whether the film will be superconducting. The transmission spectra of all resonators on each superconducting chip (4.2 K and -20 dBm drive power) were measured and theoretically fit to extract the quality factors, which are plotted in figure 15g. The extrinsic quality factors seem to roughly match the simulated values in figure 8d. We expected some disagreement since the Sonnet simulation does not account for imperfect waveguide sidewalls, spacings and kinetic inductance. The maximum intrinsic quality factor achieved was 706 and the maximum total quality factor was 379.
Overall, we find that there is consistency in T_c for a given resistivity, which is predicted well by substrate bias and N2 percentage for NbN on both oxide and high-resistivity substrates. This reflects the reproducible and robustness of our sputtering procedure. Our value of critical temperature is higher than that achieved by 10 nm thick NbN films (7.4 K) [26] and lower than 300 nm films (15.25 K) [25], which were sputtered onto high-resistivity Si and onto 400 nm oxide on p-doped Si, respectively. Since the critical temperature tends to decrease as superconducting film thickness decreases [24] (especially as the thickness reduces below 100 nm), our critical temperature of $\geq 8K$ for our 60 nm film is roughly on-par with NbN films featured in the literature. To properly compare our intrinsic quality factors with those in other studies of NbN, more measurements would likely be required. It is well-known, for instance, that the intrinsic loss depends on the power launched into the resonator and its characteristic impedance [25, 26].

6 Conclusions and Future Direction

The main objectives of this project were achieved. In this work we developed a reliable sputtering recipe to deposit thin films of NbN with a T_c of up to 8 K. Further, we have determined room temperature sheet resisitivity to be a reliable, low cost measurement for predicting the superconductivity of NbN films. The T_c is likely limited by the stiochiometry of Nb/N not being exactly one-to-one, and the film density being low. Some process adjustments in the future include lower chamber pressure, higher target power, higher RF bias, and higher substrate temperature.

Some future directions of this work include annealing NbN to improve T_c and Q [44**?** –46], using plasma-enhanced atomic layer deposition (ALD) to make very thin layers of NbN, and sputtering NbTiN. This report

is a direct springboard for pursuing latter objective. Since we have found near-ideal Lesker2 parameters for the N_2 flow and the Nb target, adding another target of Ti could be the subject of a new design of experiments (DOE) study. We have already characterized the deposition rate of Nb versus Ti in section 3.4, which would help estabish reasonable starting parameters for the DOE. In future studies, it will be important to explore new characterization methods such as, mass spectromoetry for chemical composition measurements, x-ray reflectivity for film density and thickness measurements, and high quality SEM images on the Apreo tool. Mass spectrometry and electron probe measurements may be particularly useful for determining stoichiometry, since the XPS measured stoichiometry is unreliable due to differential ion milling rates (see section 3.3). Future investigations could focus on producing a procedure for metal liftoff instead of the plasma etch, a method for directional sputtering or for etching to make NbN junctions.

7 Acknowledgements

MPM, LQ, and ES would like to thank Roger Howe and the rest of the ENGR 241 staff; our mentors Usha Raghuram, Swaroop Kommera, Graham J. Ewing, Don Gardner; and the SNF staff for making this project possible. Additionally, MPM, LQ, and ES acknowledges Amir Safavi-Naeini for project guidance, Kevin Multani for additional project guidance and providing the dxf file, and Agnetta Cleland for the Sonnet simulations and dxf file. The cryostat, PCBs, and VNA were provided by the Safavi group.

8 Supplementary Information

8.1 Why Co-planar Resonators?

The co-planar resonator design is preferred over the alternative micro-strip design [33, 47], which consist of a dielectric layer sandwiched by a conductor and a ground plane. The co-planar design, wherein the resonator is in-plane with the ground plane, allows for single-mask monolithic fabrication, reduces radiation losses and allows for more flexibility during wire bonding. As discussed in a previous E241 project [23], the co-planar resonator capacitance and characteristic impedance are given by:

$$C = 2\epsilon_0(\epsilon_r + 1)\frac{K(k_0)}{K(k_0')} \tag{8}$$

$$Z_0 = \frac{30\pi}{\sqrt{(\epsilon_r + 1)/2}}\frac{K(k_0')}{K(k_0)} \tag{9}$$

where ϵ_0 and ϵ_r are the dielectric constants of vacuo and the substrate, respectively, while $K(x)$ is the complete elliptical integral of the first kind, $k_0 = S/(S + 2W)$ and $k_0' = \sqrt{1 - k_0^2}$. The constant W is the in-plane distance between the co-planar waveguide edge and the superconducting ground plane edge. The constant S is the in-plane thickness of the co-planar waveguide. The constants W and S are shown in figure 8b.

8.2 Kinetic Inductance Nonlinearity

The main text described the behavior of a lumped element superconducting microwave resonator side-coupled to a feedline with a linear inductance determined by the in-plane geometric dimensions. However, the inductance of a circuit is not purely linear, especially when the thickness of the superconducting film is smaller. For a film with thickness t lower than its penetration depth, the surface kinetic inductance can be approximated as [26, 33]:

$$L_k = \frac{\hbar\rho}{\pi\Delta t} \tag{10}$$

where ρ is the normal state sheet resistivity per squre. The total inductance of the resonator is $L = L_0 + L_k$, where $L_0 = Z_0^2 C$ is the linear (geometric) inductance of the co-planar resonator. Higher overall inductance means greater κ_e (lower Q_e). Therefore, for thinner films we expect our simulation of Q_e to be an overestimate. Since the resonance frequency is $\omega_{res} = 1/\sqrt{LC}$, the frequency will be redshifted in the presence of kinetic inductance. Nonlinear inductance may be a significant effect in our films, considering that for NbTiN films of 300 nm thickness and $\rho \sim 170$ $\mu\Omega$-cm patterned into a similar resonator device, the kinetic inductance fraction $\alpha \equiv L_k/(L_0 + L_k)$ was 0.35 [48]. Further, NbTiN is known to have smaller kinetic inductance than NbN of the same thickness [49], and our DOE study samples are only 60 nm thick. Though kinetic inductance is a significant effect, it is not a crucial to investigate it in detail in our study. Our principle objective is to measure critical temperature and intrinsic quality factor, not make the best prediction of resonance frequency and Q_e. Kinetic inductance is relevant to applications of superconducting devices in microwave-to-optical frequency conversion, amplification or electromechanical transduction.

References

[1] Andrew E Dane, Adam N McCaughan, Di Zhu, Qingyuan Zhao, Chung-Soo Kim, Niccolo Calandri, Akshay Agarwal, Francesco Bellei, and Karl K Berggren. Bias sputtered nbn and superconducting nanowire devices. *Applied Physics Letters*, 111(12):122601, 2017.

[2] Yong Wang, Hao Li, Li-Xing You, Chao-Lin Lv, He-Qing Wang, Xing-Yu Zhang, Wei-Jun Zhang, Hui Zhou, Lu Zhang, Xiao-Yan Yang, et al. Wavelength dependence of intrinsic detection efficiency of nbn superconducting nanowire single-photon detector. *Chinese Physics B*, 28(7):078502, 2019.

[3] Yasunobu Nakamura, Hirotaka Terai, Kunihiro Inomata, Tsuyoshi Yamamoto, Wei Qiu, and Zhen Wang. Superconducting qubits consisting of epitaxially grown nbn/aln/nbn josephson junctions. *Applied Physics Letters*, 99(21):212502, 2011.

[4] Leon N Cooper and Dmitri Feldman. *BCS: 50 years*. World scientific, 2010.

[5] DM Glowacka, DJ Goldie, S Withington, H Muhammad, G Yassin, and BK Tan. Development of a nbn deposition process for superconducting quantum sensors. *arXiv preprint arXiv:1401.2292*, 2014.

[6] KL Westra, MJ Brett, and JF Vaneldik. Properties of reactively sputtered nbn films. *Journal of Vacuum Science & Technology A: Vacuum, Surfaces, and Films*, 8(3):1288–1293, 1990.

[7] Shailesh Kalal, Mukul Gupta, and Rajeev Rawat. N concentration effects on structure and superconductivity of nbn thin films. *Journal of Alloys and Compounds*, 851:155925, 2021.

[8] D Hazra, N Tsavdaris, S Jebari, A Grimm, F Blanchet, F Mercier, E Blanquet, C Chapelier, and M Hofheinz. Superconducting properties of very high quality NbN thin films grown by high temperature chemical vapor deposition. *Superconductor Science and Technology*, 29(10):105011, sep 2016.

[9] G. Lemperière and J.M. Poitevin. Influence of the nitrogen partial pressure on the properties of d.c.-sputtered titanium and titanium nitride films. *Thin Solid Films*, 111(4):339–349, 1984.

[10] Rui Sun, Kazumasa Makise, Wei Qiu, Hirotaka Terai, and Zhen Wang. Fabrication of (200) oriented tin films on si (100) substrates by dc magnetron sputtering. *IEEE Transactions on Applied Superconductivity*, 25:1–1, 01 2014.

[11] Zhen Wang, Akira Kawakami, Yoshinori Uzawa, , and Bokuji Komiyama. Superconducting properties and crystal structures of single-crystal niobium nitride thin films deposited at ambient substrate temperature. *Journal of Applied Physics*, 79, 1996.

[12] Moushab Benkahoul. *Niobium Nitride Based Thin Films Deposited by DC Reactive Magnetron Sputtering: NbN, NbSiN AND NbAIN*. PhD thesis, 2005.

[13] Sascha Krause. *Ultra-thin Niobium Nitride Films for Hot Electron Bolometer and THz Applications*. PhD thesis, 2016.

[14] Aaron D. O'Connell, M. Ansmann, R. C. Bialczak, M. Hofheinz, N. Katz, Erik Lucero, C. McKenney, M. Neeley, H. Wang, E. M. Weig, A. N. Cleland, and J. M. Martinis. Microwave dielectric loss at single photon energies and millikelvin temperatures. *Applied Physics Letters*, 92(11):112903, 2008.

[15] Tatsuya Shiino, Shoichi Shiba, Nami Sakai, Tetsuya Yamakura, Ling Jiang, Yoshinori Uzawa, Hiroyuki Maezawa, and Satoshi Yamamoto. Improvement of the critical temperature of superconducting nbtin and nbn thin films using the aln buffer layer. *Superconductor Science and Technology*, 23(4):045004, 2010.

[16] X-ray photoelectron spectroscopy (xps), Jan 2021.

[17] Alexandr V. Lubenchenko, Alexey B. Pavolotsky, Sascha Krause, Olga I. Lubenchenko, Dmitri A. Ivanov, Vincent Desmaris, and V. F. Belitsky. Native oxide on ultra-thin nbn films. 2019.

[18] P. Prieto, L. Galán, and J.M. Sanz. An xps study of nbnx prepared by ion implantation and the near-surface effects induced by ar+ bombardment. *Surface Science*, 251-252:701–705, 1991.

[19] Kareem Ali Jasim, Sameer Atta Makki, and Alia abud Almohsin. Comparison study of transition temperature between the superconducting compounds tl0.9 pb0.1 ba2ca2cu3o9-, tl0.9sb0.1ba2ca2cu3o9- and tl0.9cr0.1ba2ca2cu3o9-. *Physics Procedia*, 55:336–341, 2014. 8th International Conference on Material Sciences, CSM8-ISM5.

[20] J. T. Park, G. Friemel, Yuan Li, J.-H. Kim, V. Tsurkan, J. Deisenhofer, H.-A. Krug von Nidda, A. Loidl, A. Ivanov, B. Keimer, and D. S. Inosov. Magnetic resonant mode in the low-energy spin-excitation spectrum of superconducting $rb_2fe_4se_5$ single crystals. *Phys. Rev. Lett.*, 107:177005, Oct 2011.

[21] K W Lee, M S Kim, D H Kim, and S G Lee. Standardization of critical temperature measurement by magnetic method. *Journal of Physics: Conference Series*, 43:223–226, jun 2006.

[22] P. J. de Visser, S. Withington, and D. J. Goldie. Readout-power heating and hysteretic switching between thermal quasiparticle states in kinetic inductance detectors. *Journal of Applied Physics*, 108(11):114504, 2010.

[23] Kevin Multani, Debadri Das, and Hubert Stokowski. Superconducting parallel plate capacitors with high kinetic inductance.

[24] Kunihiro Inomata, Tsuyoshi Yamamoto, Michio Watanabe, Kazuaki Matsuba, and Jaw-Shen Tsai. Film-thickness dependence of 10 ghz nb coplanar-waveguide resonators. *Journal of Vacuum Science & Technology B: Microelectronics and Nanometer Structures Processing, Measurement, and Phenomena*, 27(5):2286–2291, 2009.

[25] Faustin W. Carter, Trupti Khaire, Clarence Chang, and Valentyn Novosad. Low-loss single-photon nbn microwave resonators on si. *Applied Physics Letters*, 115(9):092602, 2019.

[26] Cécile Xinqing Yu, Simon Zihlmann, Gonzalo Troncoso Fernández-Bada, Jean-Luc Thomassin, Frédéric Gustavo, Étienne Dumur, and Romain Maurand. Magnetic field resilient high kinetic inductance superconducting niobium nitride coplanar waveguide resonators. *Applied Physics Letters*, 118(5):054001, 2021.

[27] Timothy P. McKenna, Jeremy D. Witmer, Rishi N. Patel, Wentao Jiang, Raphaël Van Laer, Patricio Arrangoiz-Arriola, E. Alex Wollack, Jason F. Herrmann, and Amir H. Safavi-Naeini. Cryogenic microwave-to-optical conversion using a triply resonant lithium-niobate-on-sapphire transducer. *Optica*, 7(12):1737–1745, Dec 2020.

[28] E Alex Wollack, Agnetta Y Cleland, Rachel G Gruenke, Zhaoyou Wang, Patricio Arrangoiz-Arriola, and Amir H Safavi-Naeini. Quantum state preparation and tomography of entangled mechanical resonators. *Nature*, 604(7906):463–467, 2022.

[29] Shlomi Kotler, Gabriel A. Peterson, Ezad Shojaee, Florent Lecocq, Katarina Cicak, Alex Kwiatkowski, Shawn Geller, Scott Glancy, Emanuel Knill, Raymond W. Simmonds, José Aumentado, and John D. Teufel. Direct observation of deterministic macroscopic entanglement. *Science*, 372(6542):622–625, 2021.

[30] J. D. Teufel, T. Donner, Dale Li, J. W. Harlow, M. S. Allman, K. Cicak, A. J. Sirois, J. D. Whittaker, K. W. Lehnert, and R. W. Simmonds. Sideband cooling of micromechanical motion to the quantum ground state. *Nature*, 475(7356):359–363, 2011.

[31] TA Palomaki, JD Teufel, RW Simmonds, and Konrad W Lehnert. Entangling mechanical motion with microwave fields. *Science*, 342(6159):710–713, 2013.

[32] Simon Doyle, Philip Mauskopf, J Naylon, Adrian Porch, and C Duncombe. Lumped element kinetic inductance detectors. *Journal of Low Temperature Physics*, 151(1):530–536, 2008.

[33] Aditya Shreyas Kher. Superconducting nonlinear kinetic inductance devices. *California Institute of Technology Thesis*, 2017.

[34] CA Regal, JD Teufel, and KW Lehnert. Measuring nanomechanical motion with a microwave cavity interferometer. *Nature Physics*, 4(7):555–560, 2008.

[35] Peter Weber, J Guttinger, Ioannis Tsioutsios, Darrick E Chang, and Adrian Bachtold. Coupling graphene mechanical resonators to superconducting microwave cavities. *Nano letters*, 14(5):2854–2860, 2014.

[36] P.J. De Visser. Quasiparticle dynamics in aluminium superconducting microwave resonators. *TU Delft Thesis*, 2014.

[37] Patrick M. Lenggenhager Bradley Mitchell. Low frequency resonators on superconducting chips - a space-efficient lumped element design. *ETH Zurich*, 2015.

[38] A. A. Clerk, M. H. Devoret, S. M. Girvin, Florian Marquardt, and R. J. Schoelkopf. Introduction to quantum noise, measurement, and amplification. *Rev. Mod. Phys.*, 82:1155–1208, Apr 2010.

[39] C. W. Gardiner and M. J. Collett. Input and output in damped quantum systems: Quantum stochastic differential equations and the master equation. *Phys. Rev. A*, 31:3761–3774, Jun 1985.

[40] E. Alex Wollack, Agnetta Y. Cleland, Patricio Arrangoiz-Arriola, Timothy P. McKenna, Rachel G. Gruenke, Rishi N. Patel, Wentao Jiang, Christopher J. Sarabalis, and Amir H. Safavi-Naeini. Loss channels affecting lithium niobate phononic crystal resonators at cryogenic temperature. *Applied Physics Letters*, 118(12):123501, 2021.

[41] XF Meng, RS Amos, AW Lichtenberger, RJ Mattauch, and MJ Feldman. Nbn edge junction fabrication: edge profile control by reactive ion etching. *IEEE Transactions on Magnetics*, 25(2):1239–1242, 1989.

[42] A Shoji, S Kosaka, F Shinoki, M Aoyagi, and H Hayakawa. All refractory josephson tunnel junctions fabricated by reactive ion etching. *IEEE Transactions on Magnetics*, 19(3):827–830, 1983.

[43] Shuya Guo, Qi Chen, Danfeng Pan, Yaojun Wu, Xuecou Tu, Guanglong He, Hang Han, Feiyan Li, Xiaoqing Jia, Qingyuan Zhao, et al. Fabrication of superconducting niobium nitride nanowire with high aspect ratio for x-ray photon detection. *Scientific Reports*, 10(1):1–8, 2020.

[44] M Hatano, T Nishino, and U Kawabe. Effects of thermal annealing on superconducting nb and nbn films. *Journal of Vacuum Science & Technology A: Vacuum, Surfaces, and Films*, 6(4):2381–2385, 1988.

[45] C Angelkort, H Lewalter, P Warbichler, F Hofer, W Bock, and BO Kolbesen. Formation of niobium nitride by rapid thermal processing. *Spectrochimica Acta Part A: Molecular and Biomolecular Spectroscopy*, 57(10):2077–2089, 2001.

[46] Liang Tian, Ivane Bottala-Gambetta, Victor Marchetto, Manoël Jacquemin, Alexandre Crisci, Roman Reboud, Arnaud Mantoux, Gregory Berthomé, Frédéric Mercier, André Sulpice, et al. Improved critical temperature of superconducting plasma-enhanced atomic layer deposition of niobium nitride thin films by thermal annealing. *Thin Solid Films*, 709:138232, 2020.

[47] G. P. Srivastava, Mohan V. Jacob, M. Jayakumar, P. K. Bhatnagar, and N. D. Kataria. Analysis of superconducting microstrip resonator at various microwave power levels. *Journal of Applied Physics*, 81(9):6272–6276, 1997.

[48] R Barends, HL Hortensius, T Zijlstra, JJA Baselmans, SJC Yates, JR Gao, and TM Klapwijk. Contribution of dielectrics to frequency and noise of nbtin superconducting resonators. *Applied Physics Letters*, 92(22):223502, 2008.

[49] Xiaoyan Yang, Lixing You, Lu Zhang, Chaolin Lv, Hao Li, Xiaoyu Liu, Hui Zhou, and Zhen Wang. Comparison of superconducting nanowire single-photon detectors made of nbtin and nbn thin films. *IEEE Transactions on Applied Superconductivity*, 28(1):1–6, 2018.